First-principles investigation of phase stability in layered Na$_x$CrO$_2$

Jonas L. Kaufman◉ and Anton Van der Ven[*]

Materials Department, University of California, Santa Barbara, Santa Barbara, California 93106, USA

Layered oxide intercalation compounds continue to attract interest as electrode materials for Na-ion batteries. However, many of these materials undergo complex phase transitions during cycling that influence battery performance but are still not completely understood. We have conducted a first-principles study of layered Na$_x$CrO$_2$ ($0 \leqslant x \leqslant 1$) to assess phase stability between various Na-vacancy ordered phases in the O3 and P3 host structures. We predict that many of the low-energy phases belong to families of Na orderings that follow specific patterns. At high x, we identify families of vacancy row orderings in O3, which may also couple to magnetic orderings of the Cr spins. We predict similar orderings at intermediate x in P3 that contain antiphase boundaries between regions of the $x = 1/2$ ordering. In both cases, the average spacing between rows/boundaries is set by the overall composition. At $x = 0$, we find a strong preference for charge disproportionation and migration of Cr to tetrahedral sites in the intercalation layers. We obtain generally good agreement with experimental observations and rationalize key discrepancies.

I. INTRODUCTION

There is a growing effort to develop "beyond Li-ion" battery technologies that could address the world's energy storage needs at lower cost and using more widely available resources [1,2]. Na-ion batteries are one such technology that hold promise for applications such as stationary energy storage due to the far greater abundance of Na compared to Li [3]. Much research has been devoted to developing suitable materials for Na-ion batteries, particularly cathode materials [4,5]. One of the most popular classes of candidate Na-ion cathode materials is layered transition-metal oxides intercalation compounds, which generally exhibit high energy density and rate capability, and share many similarities with their well-studied Li-ion counterparts [6,7].

Various layered oxide compounds with the formula Na$_x$$MO_2$ (M = Ti, V, Cr, Mn, Fe, Co, Ni, or some combination) have been explored as electrode materials [8–23]. Among these, Na$_x$CrO$_2$ is of particular interest as a high-rate cathode material [24]. It is also considered to be inherently safe due to its exceptional thermal stability in contact with an electrolyte [25]. Despite these advantages, Na$_x$CrO$_2$ does display certain structural phase transitions and Na-vacancy ordering effects that are common to many Na layered oxide systems and generally considered detrimental [26–28]. Beyond battery applications, layered NaCrO$_2$ has also received attention from the solid-state physics community as a frustrated magnetic system [29–34].

The fully sodiated NaCrO$_2$ adopts the O3 structure (space group $R\bar{3}m$), depicted in Fig. 1(a). This structure is made up of stacked sheets of edge-sharing CrO$_6$ octahedra, which host Na in octahedral sites in the intercalation layers between them.

The Na sites form triangular lattices and do not share faces with the CrO$_6$ octahedra. There are also tetrahedral sites in the intercalation layers that share faces with the CrO$_6$ octahedra. While these sites are generally too small for Na occupation, they are able to accommodate Cr that can migrate via the shared faces. Like many O3-Na$_x$$MO_2$ materials, O3-NaCrO$_2$ transforms to the P3 structure (space group $R3m$), depicted in Fig. 1(b), upon desodiation [4,26,35,36]. This structure is obtained from O3 by a change in the stacking sequence of the CrO$_2$ sheets [18]. The Na sites form honeycomb networks, with each site sharing one face with a CrO$_6$ octahedron. While there is an energy penalty associated with the Na-Cr face sharing in P3, the honeycomb network allows for unique Na-vacancy orderings that lower the electrostatic energy contribution of Na-Na interactions relative to O3 [27,35].

The phase stability between O3 and P3 in Na$_x$CrO$_2$ has been examined in various experimental studies. Figure 2 shows several reported phase diagrams for $x > 0.5$ obtained from *ex situ* [37] or *in situ* [38–40] x-ray diffraction (XRD). These follow the same general picture of phase evolution with desodiation: The O3 structure near $x = 1$ undergoes a first-order transition to an O′3 phase near $x = 0.8$, which eventually undergoes a first-order transition to a P′3 phase at lower x. The primed phases here indicate a monoclinic distortion of the hexagonal O3 or P3 parent structure (changing the space group to $C2/m$), which typically arises due to Na-vacancy ordering over the intercalation sites. We refer to these and similar derived structures as O3- or P3-type structures.

Beyond the general similarities, there are some key discrepancies between the various experimental phase diagrams in Fig. 2. The boundaries of each single-phase region differ significantly across studies, and Jakobsen *et al.* recently reported the appearance of an extra O′3 phase (dubbed O′3-E) near $x = 0.7$ [40]. These variations across studies are not necessarily surprising, as differences in experimental parameters

---
[*]avdv@ucsb.edu

(a) O3

(b) P3
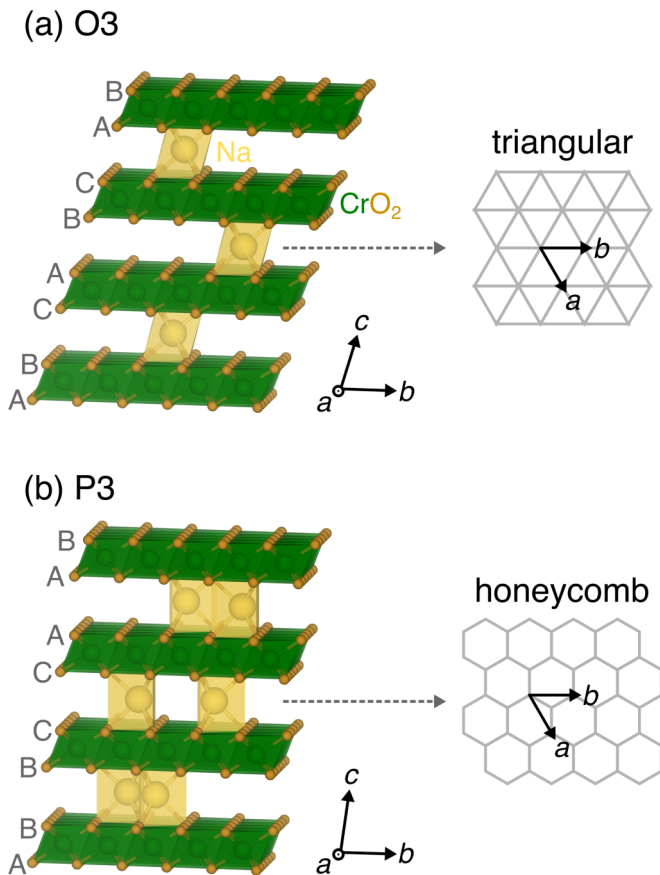
FIG. 1. The (a) O3 and (b) P3 layered structures of Na_xCrO_2, which host Na on octahedral and trigonal prismatic sites, respectively (shown at unspecified $0 < x < 1$ to illustrate Na sites and vacancies). Letters (A, B, C) indicate the oxygen stacking sequence of each structure. The two-dimensional network of available Na sites in the intercalation layers (triangular or honeycomb) is depicted for each structure.
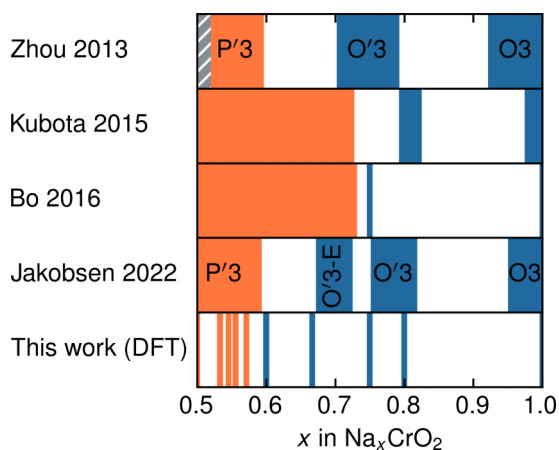
FIG. 2. Reported phase diagrams upon charge from several experimental studies, obtained from Figs. 1, 6, 3, and 3 of Refs. [38], [37], [39], and [40], respectively. Solid-colored and white blocks indicate single- and two-phase regions, respectively, while the hatched region indicates that no data were reported there. Blue and orange represent O3- and P3-type phases, respectively. The predicted ground states from this work, drawn as line compounds, are shown for comparison.

such as charge rate and composition resolution make it difficult to closely compare the results (discussed further in Sec. IV). In additional to structural phase stability, the details of Na ordering within each phase are also not well understood. Some orderings have been reported in the P'3 phase [41,42], but no comprehensive picture of ordering across composition in the O3- and P3-type structures has been established. For $x < 0.5$, Na_xCrO_2 has been found to undergo an irreversible phase transition to an O3-type phase involving charge disproportionation and migration of the Cr to tetrahedral sites in the intercalation layers, although there is some disagreement over its exact nature [37,39].

The Na_xCrO_2 system displays an interesting assortment of behavior for $0 \leqslant x \leqslant 1$. While some specific aspects have been studied using first-principles techniques [37,39,43], questions remain regarding the true equilibrium phase stability between O3- and P3-type structures, as well as the nature of Na ordering and Cr migration. Here we report on a first-principles study of phase stability between various Na-vacancy orderings in the O3 and P3 structures of Na_xCrO_2. We predict O3-type structures to be stable at high x, with the preferred orderings forming families based on the common motif of rows of vacancies that separate fully sodiated regions. Some of these orderings are also found to couple to favorable magnetic orderings. At intermediate x, we predict P3-type structures to be stable and identify families of (near) ground state orderings containing antiphase boundaries between regions of the $x = 1/2$ ordering. We also confirm a preference for Cr migration to tetrahedral sites in O3-type structures at $x = 0$, along with charge disproportionation. Our predicted phase stability and voltage profile are compared to experimental reports, and we discuss possible sources of discrepancy as well as similarities to other layered oxide systems.

II. METHODS

Density functional theory calculations were performed using the Vienna *ab initio* Simulation Package (VASP) [44–47]. Projector augmented wave (PAW) pseudopotentials were used (Na pv, Cr pv, and O) [48,49]. The plane-wave energy cutoff was chosen to be 600 eV, and the Brillouin zone was sampled with Γ-centered Monkhorst-Pack k meshes [50] of density 34 Å along each reciprocal lattice vector (increased to 40 Å for calculating density of states). All calculations were spin-polarized and initialized in the ferromagnetic (FM) state, unless otherwise noted. All structures were relaxed until forces were less 0.02 eV/Å. Final static calculations were run using the linear tetrahedron method to obtain reliable total energies [51]. The SCAN meta-GGA exchange-correlation functional [52,53] was used because it has been shown to provide accurate predictions of voltage, structural parameters, and phase stability in related layered oxide systems [54–60]. Some calculations were also run with PBE [61] and PBE + U [62] (with $U = 3.5$ eV for Cr) for comparison. Unless otherwise noted, all reported properties and structures are from calculations using the SCAN functional. All crystal structure visualizations were created using VESTA [63].

Symmetrically distinct Na-vacancy orderings in the O3 and P3 host structures of Na_xCrO_2 were enumerated using the Clusters Approach to Statistical Mechanics (CASM) software

package [64–67]. DFT energies were calculated for 228 O3 configurations and 273 P3 configurations. Energies were calculated for an additional 37 configurations of O3-CrO$_2$ in which one third of the Cr have been moved to tetrahedral sites in the intercalation layers (all such structures in supercells of volume up to six times the primitive cell volume). We also enumerated and calculated DFT energies for collinear magnetic orderings of the Cr spins within the predicted O3 and P3 ground states at select compositions.

CASM was used to construct cluster expansion effective Hamiltonians for the O3 and P3 structures (not considering magnetic ordering or Cr migration), which we employed to iteratively predict candidate ground state structures whose energies were subsequently calculated with DFT. Details of the cluster expansions are provided in Sec. S1 of the Supplemental Material [68] (see, also, Refs. [69–71] therein). These cluster expansions were also used to run Monte Carlo simulations of finite-temperature phase stability, the details of which are provided in Sec. S2 of the Supplemental Material [68].

Voltages were calculated using the Nernst equation [72]

$$V = -\frac{\mu_{Na} - \mu_{Na}^{\circ}}{e}, \qquad (1)$$

where μ_{Na} is the chemical potential of Na in Na$_x$CrO$_2$, μ_{Na}° is the chemical potential of the reference anode (taken to be body-centered cubic Na metal [73]), and e is the elementary charge.

III. RESULTS

A. Phase stability

Figure 3(a) shows the calculated zero-temperature formation energies of Na$_x$CrO$_2$ configurations in the O3 and P3 structures, referenced to O3-CrO$_2$ and O3-NaCrO$_2$ (FM). Also included are energies of the most favorable magnetic orderings found in O3 at $x = 1$, $x = 4/5$, and $x = 3/4$, as well as O3-type configurations at $x = 0$ with one third of the Cr migrated to tetrahedral sites in the intercalation layers. The global formation energy convex hull determines the zero-temperature phase stability. To more easily compare energies of configurations close to the hull, distances above the hull (excluding the Cr migration configurations) are also plotted in Fig. S3 of the Supplemental Material [68]. We predict O3-type configurations to be stable for $3/5 \leqslant x \leqslant 1$, and P3-type configurations to be stable for $1/2 \leqslant x \leqslant 4/7$. At $x = 0$ an O3-type configuration with tetrahedral Cr is predicted to have the lowest energy. Our predicted phase stability for $x \geqslant 1/2$ is generally in good agreement with experimental studies (Fig. 2), which report O3-type phases appearing around $x = 0.8$ upon desodiation and P3-type phases appearing at or just below $x = 0.6$ (according to Zhou *et al.* [38] and Jakobsen *et al.* [40]). We do predict a narrower two-phase region between P3-type and O3-type than has been reported experimentally, with O3-type phases predicted to be stable down to $x = 3/5$. The results of our grand canonical Monte Carlo simulations (summarized in Sec. S2 of the Supplemental Material [68]) also suggest that the O3-type regime extends to even lower x with increasing temperature, while the P3-type regime becomes narrower.
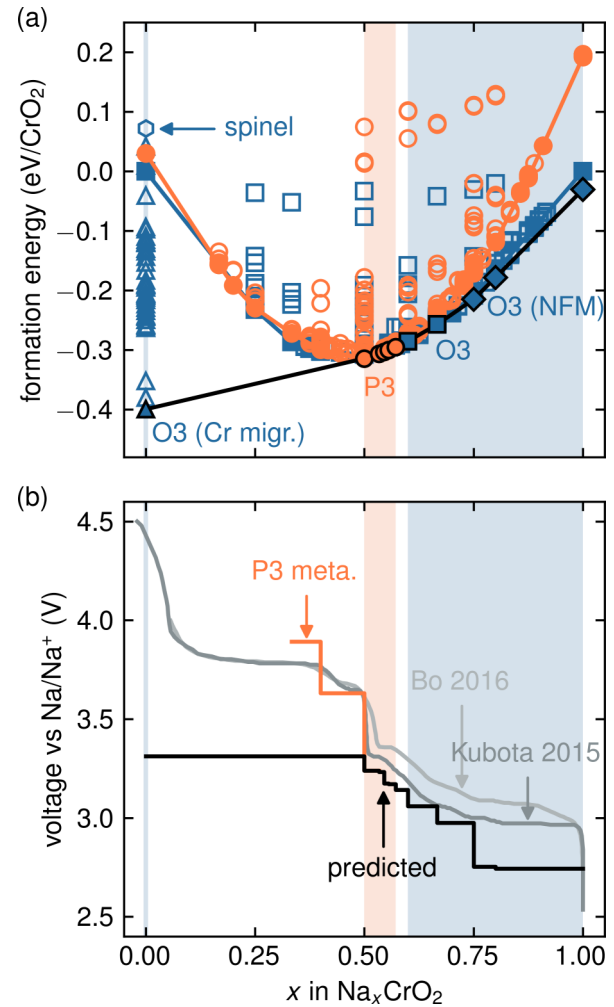
FIG. 3. (a) Calculated formation energies of O3-type and P3-type configurations versus composition. For O3, FM configurations are marked by squares while non-FM configurations are marked by diamonds, and configurations with Cr migrated to tetrahedral sites are marked by triangles. Filled markers with lines connecting them indicate configurations on the local convex hull of each host structure (not accounting for magnetic ordering or Cr migration). The global convex hull is outlined in black. Shaded regions indicate where each host structure is globally stable. (b) Predicted voltage curve from DFT (black) compared to experimental voltage curves from first charge reported by Bo *et al.* [39] and Kubota *et al.* [37] (light and dark gray). The composition of the voltage curve from Kubota *et al.* has been transformed as $x \to 1.09x - 0.09$. Part of the predicted metastable P3 voltage curve is also shown (orange).

While we performed most calculations with FM alignment of the Cr spins, we did explore non-FM magnetic configurations at select compositions in O3 and P3, the energies and net magnetic moments of which are shown in Fig. S4 of the Supplemental Material [68]. At $x = 1$ in both O3 and P3, an antiferromagnetic (AFM) in-layer ordering (Fig. S5 of the Supplemental Material [68]) is predicted to be most stable. This configuration is 31 meV/CrO$_2$ and 43 meV/CrO$_2$ lower in energy than the FM configuration in O3 and P3, respectively. The predicted preference for AFM ordering at $x = 1$ is consistent with experimental reports of the magnetic

behavior of NaCrO$_2$, which displays AFM direct exchange interactions resulting from overlap of the Cr t_{2g} orbitals [30]. The collinear AFM ordering we identify is almost certainly not the true ground state, however, as NaCrO$_2$ is a known triangular Heisenberg antiferromagnet with more exotic low-temperature magnetic behavior [30–32]. In O3, we find non-FM configurations are also preferred at $x = 4/5$ (10 meV/CrO$_2$ below FM) and $x = 3/4$ (6 meV/CrO$_2$ below FM), while no such preference is found in P3 at $x = 2/3$ or $x = 1/2$. It is somewhat intuitive that the preference for AFM ordering would diminish with decreasing x. As Na is removed and Cr is oxidized from 3+ (d^3) toward 4+ (d^2), the hopping of aligned spins between t_{2g} orbitals of neighboring Cr ions would no longer be completely suppressed due the Pauli exclusion principle [74]. We emphasize that we expect the material to be paramagnetic at room temperature, as the reported Néel temperature of NaCrO$_2$ is 41 K [30].

Figure 3(b) shows the equilibrium voltage derived from the calculated zero-temperature formation energies in Fig. 3(a). The multitude of steps in the predicted voltage curve correspond to Na-vacancy orderings in O3 and P3, which we examine in detail in Sec. III B. The O3-CrO$_2$ configuration with tetrahedral Cr produces a large two-phase voltage plateau at around 3.3 V; however, following the convex hull of metastable configurations in P3 (which is observed down to $x \approx 0.4$ experimentally [37,39]) instead reveals a large voltage step at $x = 1/2$. Experimentally measured first-charge voltage curves reported by Kubota *et al.* [37] and Bo *et al.* [39] are also shown in Fig. 3(b) for comparison. For $x > 1/2$, the agreement between the predicted and experimental voltage curves is quite close, with the many steps in the predicted curve matching the sloped section measured experimentally. At high x, we expect that magnetic entropy would lower the free energy of the O3-type phases at room temperature and raise the corresponding voltage to be closer to the experimental value. At low x, we predict a lower voltage for Cr migration to tetrahedral sites than the 3.8 V plateau observed experimentally. We address this discrepancy and present further details of the Cr migration mechanism in Sec. III C. The predicted metastable voltage curve of P3-type phases, however, provides excellent correspondence with experiment, reproducing the observed step at $x = 1/2$.

B. Ground state orderings

As shown in Fig. 3, there are numerous (near) ground state configurations predicted in the O3 and P3 structures. By closely examining these Na-vacancy orderings, we are able to identify overarching patterns that connect them. Note that we generally do not distinguish between the parent O3/P3 structures and any derived structures (e.g., O′3/P′3) in our results, referring to O3/P3-type structures simply as O3/P3 structures or configurations. The various primed phase labels are more useful in cases such as refinement of experimental diffraction data than in atomistic calculations, as in the latter the atomic positions (and therefore the symmetry group) are known exactly for each configuration. The relaxed crystal structures, along with all of our DFT calculation data, are made available to facilitate future studies (Sec. S3 of the Supplemental Material [68]).
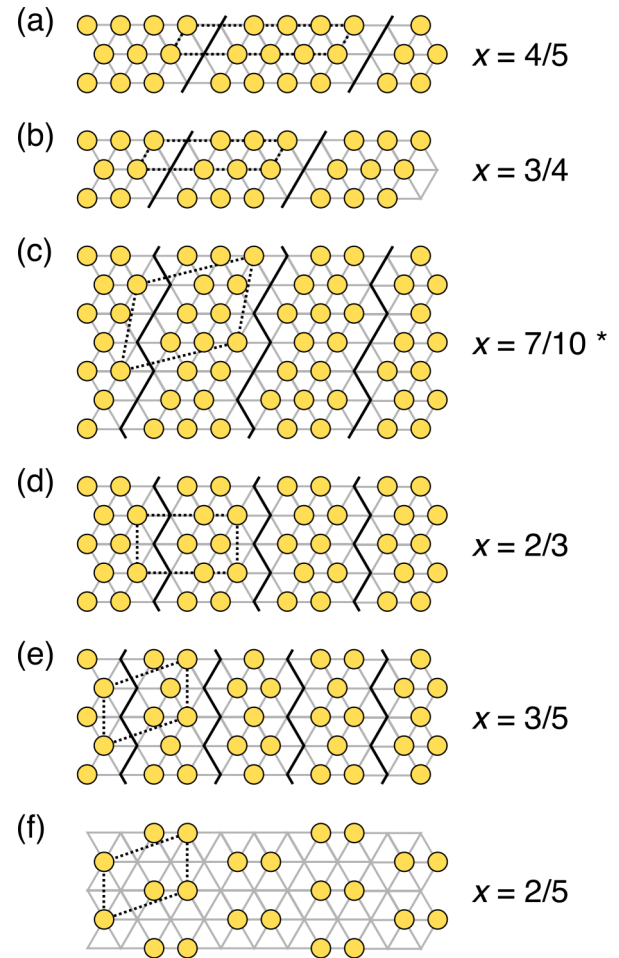
FIG. 4. Select predicted ground state Na orderings on the triangular lattice in O3 [shown in Fig. 1(a)]. Dotted black lines indicate the unit cells and solid black lines indicate rows of vacancies between fully sodiated regions. Asterisk indicates that the ordering is on the hull of FM configurations, but is displaced from the hull when accounting for non-FM configurations.

1. O3 orderings

Key orderings in the O3 structure are shown in Fig. 4. The ground state orderings immediately below $x = 1$, at $x = 4/5$ and $x = 3/4$, contain straight rows of vacancies between fully sodiated regions [Figs. 4(a) and 4(b)]. As previously mentioned, both of these configurations prefer non-FM orderings of the Cr spins, which are shown in Fig. 5. These magnetic orderings are coupled to distortions of the CrO$_2$ sheets caused by the Na orderings, such that the distance between neighboring Cr ions is smaller when their spins are antialigned than it is when they are aligned. We also identify an ordering at $x = 7/9$ (not shown) that interpolates the $x = 3/4$ and $x = 4/5$ orderings, alternating between three and four rows of Na between vacant rows. It is predicted to lie just 0.1 meV/CrO$_2$ above the FM convex hull. This suggests that there could be a "Devil's staircase" of many orderings with varying average spacing between vacant rows, as was previously predicted to be stable in O3-Na$_x$CoO$_2$ and labeled the θ family [75]. Like in that system, these orderings could correspond to the
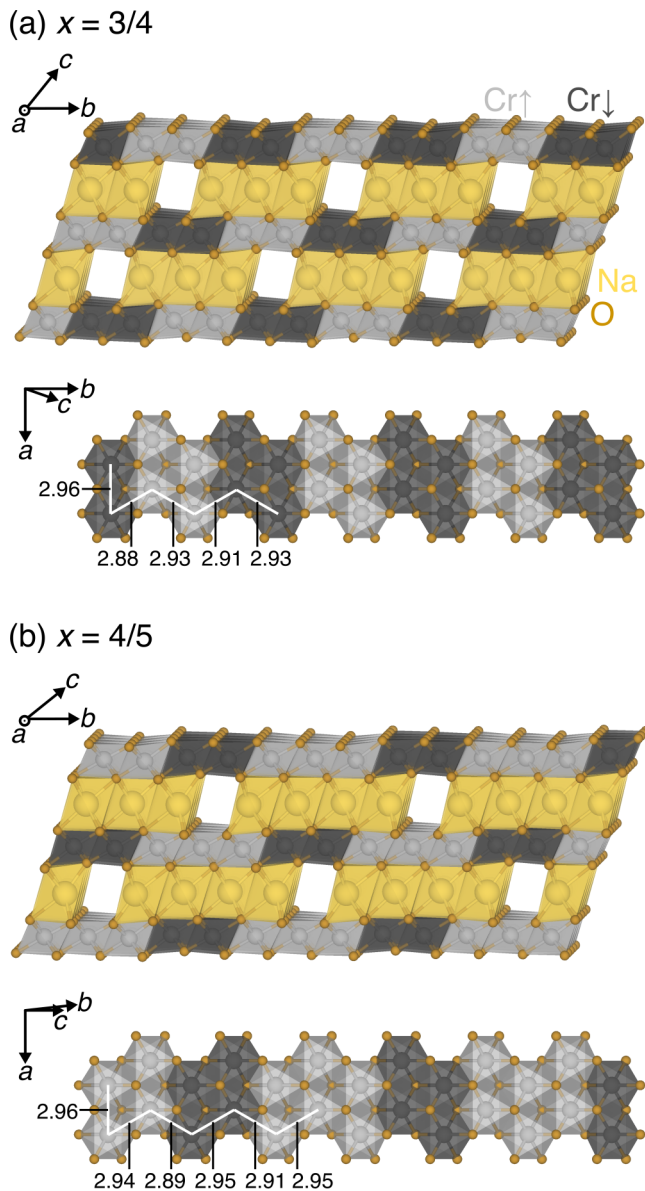
FIG. 5. Relaxed structures of the lowest-energy non-FM configurations found in O3 for (a) $x = 3/4$ and (b) $x = 4/5$, viewed from the side and top. Spin up/down Cr are shown as light/dark gray. The unique nearest-neighbor Cr-Cr pair distances for each structure (in Å) are labeled.

monoclinically distorted O′3 phases observed experimentally at high x (around 0.75–0.8) in Na_xCrO_2 (Fig. 2).

At lower compositions in O3, the preferred orderings also consist of rows of vacancies between fully sodiated regions; however, the rows are no longer completely straight. The $x = 7/10$ ordering shown in Fig. 4(c), which lies on the hull of FM configurations in O3, contains periodic kinks in the vacant rows. In the ground states at $x = 2/3$ and $x = 3/5$ [Figs. 4(d) and 4(e)], the kinks are as closely spaced as possible, and these orderings only differ in the spacing between the rows of vacancies. As with the θ family at higher compositions, there could potentially be a staircase of orderings in this composition regime with varying spacing of vacant rows and/or varying density of kinks along the vacant rows. Thus we
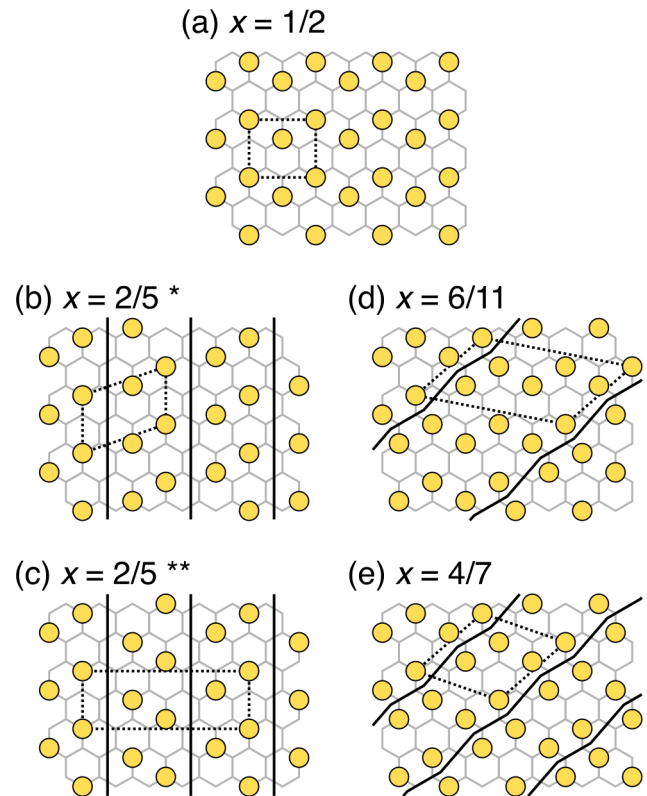
FIG. 6. Select predicted (near) ground state Na orderings on the honeycomb network in P3 [shown in Fig. 1(b)]. Dotted black lines indicate the unit cells and solid black lines antiphase boundaries between regions of the $x = 1/2$ ordering (a). A single asterisk indicates that the ordering is above the global hull, while a double asterisk indicates that the ordering is also above the P3 hull.

identify two qualitatively distinct families of orderings in O3 above $x = 1/2$, based on either straight or corrugated rows of vacancies. The latter could possibly explain the second O′3 phase around $x = 0.7$ recently reported by Jakobsen *et al.* [40] (Fig. 2).

2. P3 orderings

Figure 6 shows important orderings predicted in the P3 structure. The ground state at $x = 1/2$ [Fig. 6(a)] is particularly stable, as demonstrated by the large step it produces in the P3 voltage curve [Fig. 3(b)]. This ordering, which we refer to as ζ, is also favored by several other layered Na and K intercalation compounds in the P3 and P2 structures [4,23,41,58,76–78]. Its stability is attributed to increased Na-Na distances relative to alternate arrangements, which minimize the electrostatic repulsion between the ions. Yabuuchi *et al.* confirmed the ζ ordering experimentally in P′3−$Na_{0.5}CrO_2$ via synchrotron XRD, and also found that it undergoes a disordering transition upon heating at 150–200 °C [41]. We estimate from our Monte Carlo simulations that the ζ ordering disorders at around 475 K (202 °C) (Fig. S2 of the Supplemental Material [68]), which is in close agreement with the experimentally determined transition temperature.

Above $x = 1/2$ in P3, we predict that the highly favorable ζ ordering is preserved locally, and that additional Na are accommodated along antiphase boundaries (APBs). The ground state ordering at $x = 6/11$, shown in Fig. 6(d), illustrates this motif. There are also predicted ground states at $x = 8/15$ and $x = 5/9$ (not shown) that differ only in the average spacing between APBs. The ground state at $x = 4/7$, which we refer to as the η ordering, has the smallest separation of APBs that was found to be stable [Fig. 6(e)]. As with the vacancy row orderings identified in O3, these APB-based orderings allow for essentially arbitrary variation in composition controlled by the average density of APBs. This particular staircase of orderings was also predicted in P3-Na$_x$CoO$_2$ and labeled the ζ^+ family [75]. Above $x = 4/7$, we also find ground states at $x = 8/13$ and $x = 2/3$ (not shown) that are common to P3-Na$_x$CoO$_2$ and belong to a staircase of orderings containing APBs between variants of the η ordering, referred to as the η^+ family [75]. However, these are not found to be globally stable here.

Chen *et al.* recently reported similar APB-based orderings for $1/2 \leqslant x \leqslant 2/3$ in Na$_x$CrO$_2$ determined from *in situ* XRD [42]. They identified superstructures consisting of regions of the ζ ordering separated by different APBs from those presented here. Though certainly not an exhaustive comparison, we calculated the energies of two such orderings from Chen *et al.* at $x = 5/9$ and $x = 2/3$ to lie 7 meV/CrO$_2$ and 8 meV/CrO$_2$ above the hull of our calculated structures, respectively. Due to the large supercell sizes of these orderings, we did not test different relative stackings within the three-dimensional crystal, which could potentially yield lower energies (as we discuss later in this section). However, such small energy differences indicate that the P3 voltage profile would likely not be significantly affected by choosing one ordering scenario over the other. It is possible that the orderings we predict could also be compatible with the reported XRD data, as the nature of their unit cells, which determine peak positions, is similar to that of the orderings from Chen *et al.* Careful XRD refinement analysis, perhaps even considering additional candidate APB types beyond those presented here and by Chen *et al.*, would be required to determine the most probable ordered superstructures.

Below $x = 1/2$, we predict one ground state ordering in P3 at $x = 2/5$, shown in Fig. 6(b). Like the P3 orderings above $x = 1/2$, this ordering can be viewed as regions of the ζ ordering separated by APBs; however, this type of APB accommodates vacancies rather than additional Na. This again suggests that there could be numerous (near) ground states between $x = 1/2$ and $x = 2/5$ with varying average densities of APBs. For instance, there is one ordering at $x = 4/9$ with more widely spaced APBs (not shown) that has a calculated energy just 0.5 meV/CrO$_2$ above the P3 convex hull. Interestingly, these orderings are slightly different from those predicted in P3-Na$_x$CoO$_2$, which are based on a different type of APB and form a staircase of orderings below $x = 1/2$ labeled the ζ^- family. This other APB type is shown in the alternative $x = 2/5$ ordering in Fig. 6(c). In Na$_x$CrO$_2$, we calculate the energy of this ordering to lie 6 meV/CrO$_2$ above that of the preferred ordering in Fig. 6(b). We note, however, that the energy of the latter is 3 meV/CrO$_2$ above that of the O3 ground state at $x = 2/5$ [Fig. 4(f)], which contradicts
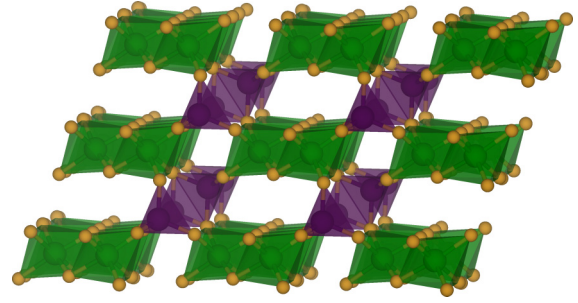
FIG. 7. Relaxed structure of the predicted ground state O3-CrO$_2$ configuration ($x = 0$) with one third of the Cr occupying tetrahedral sites in the intercalation layers.

experimental observations of a P3-type phase down to $x \approx 0.4$ [39]. While this may signify an incorrect prediction of the SCAN functional, the predicted difference in energy between P3 and O3 is very small and there is undoubtedly a sizable kinetic barrier for the stacking sequence transformation from P3 to O3.

One subtlety we have disregarded in presenting these two-dimensional orderings is their stacking within the three-dimensional crystal. The influence of stacking on the energy of O3 orderings in various Na transition metal oxides was studied by Toumar *et al.*, who determined that, while it is generally less important than intralayer Na ordering, the effect of stacking is not necessarily negligible [43]. To investigate this effect for our predicted P3 orderings, we calculated the energies of all distinct single-layer stackings of key P3 ground states at $x = 2/5$, $x = 1/2$, $x = 4/7$, and $x = 2/3$ (Fig. S6 of the Supplemental Material [68]). The energy range of different stackings is less than 10 meV/CrO$_2$ at $x = 1/2$, $x = 4/7$, and $x = 2/3$, but is 20 meV/CrO$_2$ at $x = 2/5$. These results suggest that stacking does indeed have a significant effect, which should be considered in more detailed studies involving the orderings we have identified here.

C. Cr migration

As shown in Fig. 3(a), interlayer Cr migration to tetrahedral sites is predicted to be favorable in O3-CrO$_2$. The corresponding predicted ground state structure is shown in Fig. 7. In this structure, one third of the Cr have migrated to the intercalation layers, forming rows of tetrahedral Cr sites. Examining the calculated partial densities of states (Fig. 8), we find that the tetrahedral Cr contribute minimally to the Cr d states immediately below the Fermi energy, consistent with an oxidation state of $6+$ (d^0). These states represent a total of two electrons per CrO$_2$, or three electrons per octahedral Cr, in line with an oxidation state close to $3+$ (d^3) for the octahedral Cr. Thus our results agree with the expected disproportionation of Cr$^{4+} \rightarrow \frac{2}{3}Cr^{3+} + \frac{1}{3}$Cr^{6+}.

Although the structure in Fig. 7 has the lowest energy among those at $x = 0$ considered in this work, it is unlikely that it is accessed during the electrochemical extraction of Na. Bo *et al.* observed that the plateau at 3.8 V corresponds to the formation of an O3-Na$_\delta$CrO$_2$ phase with hexagonal ($R\bar{3}m$) symmetry, one third of the Cr migrated to tetrahedral sites, and a small amount of residual Na ($\delta = 0.04$) [39]. While
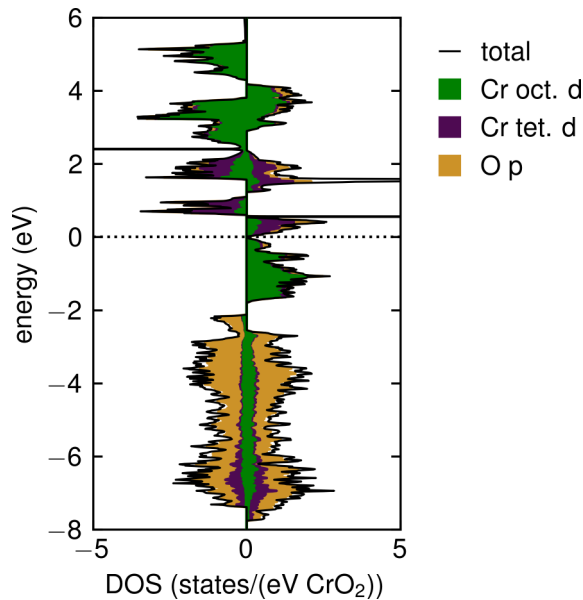
FIG. 8. Total and partial densities of states for predicted ground state O3-CrO_2 structure with Cr migration to tetrahedral sites (Fig. 7).

the structure in Fig. 7 is consistent with the observed charge disproportionation and migration of Cr, the row ordering of tetrahedral sites (Fig. 7) clearly breaks the $R\bar{3}m$ symmetry. The true structure formed experimentally likely contains a disordered arrangement of tetrahedral Cr sites.

There are also kinetic effects that would hinder the complete extraction of Na. In O3, Na hops between octahedral sites via the intermediate tetrahedral sites, but if a significant number of those sites are occupied by Cr then some Na could become trapped in the structure. However, with 1/3 of the Cr in tetrahedral sites, 5/6 of the tetrahedral sites in the intercalation layer would still be vacant, suggesting that Na diffusion channels would not be completely blocked. The more relevant effect is likely the contraction of the interlayer spacing near $x = 0$, which is known to inhibit diffusion by significantly increasing ion migration barriers [79–82]. The structure shown in Fig. 7 has an average interlayer spacing (between the oxygen above and below the intercalation layer) of 2.49 Å, compared to 3.16 Å for O3-$NaCrO_2$. This is also smaller than the interlayer spacing of O3-CrO_2 without Cr migration (2.58 Å), indicating that the presence of tetrahedral Cr contributes to an even more severe contraction. While these effects are often acknowledged as preventing ion reinsertion [8,10,17,37,39], they may also explain why a small amount of Na remains. If the kinetically accessible $Na_\delta CrO_2$ phase has a significantly higher formation energy than the CrO_2 phase we have identified, then it would raise the voltage of the two-phase plateau closer to the value measured experimentally.

Bo *et al.* reported that the O3-$Na_\delta CrO_2$ phase serves as an intermediate for a transition to a rocksalt CrO_2 phase (with Cr occupying half of the available octahedral sites) [39]. This differs from an earlier experimental report by Kubota *et al.*, who described a single O3-$Na_\delta CrO_2$ phase (with $\delta = 0.06$) containing both tetrahedral and octahedral Cr in the intercalation layers, rather than a two-phase mixture with rocksalt [37].

In light of this discrepancy, we considered a rocksalt-derived structure with stoichiometry CrO_2 in which Cr adopts the same ordering as Mn in spinel $LiMn_2O_4$ (shown in Fig. S7 of the Supplemental Material [68]). This spinel-like structure can be viewed as a particular one-half vacancy ordering on the rocksalt parent structure. As shown in Fig. 3(a), we find that the formation of the spinel-like structure is unfavorable, with its energy lying 72 meV/CrO_2 above that of the O3-CrO_2 reference structure (without tetrahedral Cr). Other Cr-vacancy arrangements would need to be considered to determine definitively whether there is a more stable (dis)ordered rocksalt phase of CrO_2. Importantly, Bo *et al.* reported short-range Cr-vacancy ordering in the rocksalt phase evidenced by diffuse scattering in the electron diffraction pattern [39], a phenomenon frequently discussed within the disordered rocksalt materials literature [83–86]. While there is clearly a strong thermodynamic driving force for charge disproportionation and migration of Cr to tetrahedral sites, kinetic effects may very well lead to subsequent coproportionation and rocksalt formation, which could be understood through further computational studies.

IV. DISCUSSION

In this first-principles study, we have examined phase stability among various ion orderings in the O3 and P3 layered host structures of $Na_x CrO_2$ ($0 \leqslant x \leqslant 1$). O3 is found to be stable at high Na concentrations while P3 appears at intermediate ones. We identify many low-energy Na-vacancy orderings which can be organized into families, each based on a specific motif. In O3 the orderings contain rows of vacancies that serve as boundaries between fully sodiated regions, and in P3 the orderings contain APBs between regions of the particularly favorable $x = 1/2$ ordering (ζ). In each case, variations in the boundary density produce variations in the overall composition. The predicted phase stability regions and voltage are mostly consistent with experimental reports. We also confirm a preference for AFM ordering at high x and for Cr migration to tetrahedral sites in the intercalation layers of O3 at low x.

The main discrepancy between our predictions and experimental reports is in precisely where the transition from O3- to P3-type stacking occurs upon desodiation (see Fig. 2). At zero temperature, we predict that O3 is stable down to $x = 3/5 = 0.6$, which marks the start of a two-phase region with P3 at $x = 4/7 \approx 0.57$. Some experimental studies, however, report a P3 phase at compositions as high as $x \approx 0.7$ [37,39]. There are also reports of P3 not appearing until $x \approx 0.6$ [38,40], but with a significantly wider two-phase region with O3 than we predict. While it is possible that we could have missed important configurations in P3, we did verify that there were no new ground state orderings predicted by our cluster expansion for $3/8 \leqslant x \leqslant 3/4$ in supercells of volume 10 times the primitive cell volume or less. It is therefore unlikely that any dramatically more stable configurations were omitted. Furthermore, previous DFT studies similarly found O3 to be more stable than P3 at $x = 2/3$ [39] and $x = 3/5$ [37]. We also see no evidence that magnetic ordering lowers the energies of P3 configurations for intermediate x (Fig. S4 of the Supplemental Material [68]).

There are several possible explanations for the discrepancy between the predicted phase boundaries of P3 and those inferred from experimental observations. One possibility is that P3 is further stabilized by entropy at finite temperature. Our Monte Carlo simulation results, however, show that configurational entropy actually serves to stabilize O3 even more (Fig. S1 of the Supplemental Material [68]), though we do caution that the cluster expansion and Monte Carlo approach may not be able to capture collective excitations in the ordered phases of P3, such as rearrangements of APBs [87]. We have not considered vibrational entropy, which could potentially be relevant. Yabuuchi *et al.* reported the somewhat unusual decomposition of $P'3-Na_{0.5}CrO_2$ into Na-rich and Na-free P3 phases upon heating, which could indicate the importance of phonons at high (and low) x [41].

It is also important to recognize that the various experimental studies we reference were not necessarily designed to determine the O3/P3 phase boundaries precisely. Furthermore, differences in experimental parameters greatly complicate comparisons among the literature results and our study. The studies summarized in Fig. 2 employed different charge rates and composition resolutions, which are listed in Table S2 of the Supplemental Material [68]. Zhou *et al.* [38] and Jakobsen *et al.* [40] used relatively fast charge rates (C/12 and C/15, respectively), which could have delayed the transition to $P'3$ on charge and/or widened the composition region over which it occurred. In some cases, most notably the *ex situ* measurements from Kubota *et al.* [37], the relatively low composition resolution prevents a precise determination of the transition composition range. Bo *et al.* [39] performed measurements at a slower charge rate of C/50 and also reported the narrowest two-phase region ($\Delta x \approx 0.02$) among the studies considered. This suggests that the stacking sequence transition upon charge is kinetically limited and that the sharper transition seen at slower rates is more indicative of the equilibrium thermodynamics. Further experiments, performed at slow charge rate and high composition resolution, may be necessary to precisely understand the equilibrium phase stability.

In assessing our predictions, it is also informative to examine their sensitivity to the particular DFT method used. We took the FM ground states from each structure as determined by SCAN and recalculated their energies using PBE and PBE $+ U$, with $U = 3.5$ eV for Cr. This value of U is used throughout the literature [37,39,42,88], allowing us to compare to other computational results more clearly. The resulting formation energies and voltage curves are shown in Fig. S8 of the Supplemental Material [68], compared to our SCAN results. While we acknowledge that a more rigorous comparison would involve a recalculation of the energies of many/all configurations with each DFT method, our analysis still provides some useful insights. Compared to SCAN, PBE yields a wider stability region for the P3 structure that extends up to $x = 8/13$ (versus $x = 4/7$ with SCAN). O3 is still predicted to be more stable than P3 at $x = 2/5$, but by a mere 0.1 meV/CrO_2 (versus 3 meV/CrO_2 with SCAN). The predicted voltage from PBE is about 1 V lower than the SCAN voltage, which is consistent with benchmarking results for transition-metal oxides intercalated with Li [55]. The O3-CrO_2 structure containing tetrahedral Cr is less stable

with PBE, producing a higher cutoff voltage (relative to the rest of the voltage curve) than with SCAN. With PBE $+ U$, we find that many of the SCAN ground states are displaced from the formation energy convex hull, and that the P3 stability region is even narrower (Fig. S8(c), Supplemental Material [68]). This produces a voltage curve that is quite different in shape from the SCAN and PBE curves, even though it is close in value to the voltages from SCAN and experiment. It is known that the addition of a U term can significantly alter ground state predictions by inducing charge ordering [89]. Our comparison highlights the advantage of SCAN: It seems to provide reliable predictions of both phase stability and average voltage without requiring an empirical parameter such as U. For future studies, note that the recently developed r^{2}SCAN functional offers improved numerical performance while preserving the accuracy of SCAN [90,91].

We find that Na_xCrO_2 displays many similarities to related layered oxide systems, as well as some key differences. The APB-based P3 orderings predicted here are largely the same as those predicted by first-principles studies of Na_xCoO_2, K_xCoO_2, and K_xCrO_2 [58,75,78]. This suggests that their stability arises from simple electrostatic interactions rather than specific chemical effects. The vacancy row orderings we identify in O3 are also the same as those predicted in Na_xCoO_2 [75]. In the analogous K systems, however, these structures relax to "M" phases containing a mixture of octahedral and prismatic K in the same intercalation layer [58,78], which has been attributed to the increased electrostatic repulsion between K^+ ions compared to Na^+. A key distinction of the Na_xCrO_2 system is the relatively lower stability of P3 relative to O3 at intermediate x. Here we predict P3 to be stable up to $x = 4/7$, while it is found to be stable up to $x = 2/3$ in the Co and K analogs [58,75,78]. This behavior can be explained by considering the competing electrostatic repulsions that serve to (de)stabilize P3. While the intercalant ions in P3 share faces with transition-metal ions in the neighboring layers (which they do not in O3), this penalty is balanced by a reduction of intralayer repulsions between intercalant ions by their arrangement on the honeycomb networks [35]. In the case of K_xCoO_2 and K_xCrO_2, the repulsions between K^+ ions are strong enough that changing the transition-metal identity does not noticeably alter the stability of P3. In the case of Na_xCoO_2 and Na_xCrO_2, however, the larger ionic radius of Cr compared to Co in the same oxidation state [54] yields larger distances between intercalation sites, making the the effects of intralayer Na-Na repulsions, and thus the stability of P3, less pronounced.

The ordering patterns we have identified likely have significant consequences for ion diffusion. Highly ordered phases tend to lead to a significant reduction in the diffusion coefficient [79]; however, this may not be true of the APB-based orderings in P3 predicted here. In P3-Na_xCoO_2, APBs have been theorized to facilitate diffusion via their collective motion through the intercalation layers [87]. The simulated diffusion was found to be Fickian, with a strong dependence of the diffusion coefficient on the Na concentration (corresponding to the APB density) [92]. The orderings we predict for $x > 1/2$ in Na_xCrO_2 are identical to those predicted in Na_xCoO_2, and although we predict a slightly different type of APB for $x < 1/2$, we believe that a similar diffusion mechanism

based on APB migration may play a key role in both regimes in this system. Comparable mechanisms may also be relevant in the vacancy row orderings found in O3 at Na high concentrations. We do acknowledge that the orderings in Na_xCrO_2 are likely more tolerant to defects than those in Na_xCoO_2 due to the increased in-layer lattice parameter, which may enable additional diffusion mechanisms.

V. CONCLUSION

In this study, we investigated phase stability between the O3 and P3 structures of layered Na_xCrO_2 and the nature of Na ordering within them. We identified several families of low-energy orderings: Some in O3 at high x containing rows of vacancies and some in P3 at intermediate x containing antiphase boundaries, which both enable smooth variations in composition. Similar orderings have been predicted in related Na and K intercalation compounds, and have important consequences for Na diffusion. In O3, we considered migration of Cr to tetrahedral sites in the intercalation layers at $x = 0$ and found a strong energetic preference tied to charge disproportionation. We have discussed how our findings may clarify discrepancies in the literature, specifically regarding the O3 $\rightarrow$ P3 transition upon desodiation and the Cr migration mechanism at low x. These results serve as fundamental groundwork for future computational and experimental studies of this promising electrode material.

[1] Y. Tian, G. Zeng, A. Rutt, T. Shi, H. Kim, J. Wang, J. Koettgen, Y. Sun, B. Ouyang, T. Chen, Z. Lun, Z. Rong, K. Persson, and G. Ceder, Promises and challenges of next-generation beyond Li-ion batteries for electric vehicles and grid decarbonization, Chem. Rev. **121**, 1623 (2021).

[2] O. Sapunkov, V. Pande, A. Khetan, C. Choomwattana, and V. Viswanathan, Quantifying the promise of 'beyond' Li-ion batteries, Transl. Mater. Res. **2**, 045002 (2015).

[3] K. Kubota, M. Dahbi, T. Hosaka, S. Kumakura, and S. Komaba, Towards K-ion and Na-ion batteries as "beyond Li-ion", Chem. Rec. **18**, 459 (2018).

[4] N. Yabuuchi, K. Kubota, M. Dahbi, and S. Komaba, Research development on sodium-ion batteries, Chem. Rev. **114**, 11636 (2014).

[5] C. Delmas, Sodium and sodium-ion batteries: 50 years of research, Adv. Energy Mater. **8**, 1703137 (2018).

[6] M. H. Han, E. Gonzalo, G. Singh, and T. Rojo, A comprehensive review of sodium layered oxides: Powerful cathodes for Na-ion batteries, Energy Environ. Sci. **8**, 81 (2015).

[7] M. D. Radin, S. Hy, M. Sina, C. Fang, H. Liu, J. Vinckeviciute, M. Zhang, M. S. Whittingham, Y. S. Meng, and A. Van der Ven, Narrowing the gap between theoretical and practical capacities in Li-ion layered oxide cathode materials, Adv. Energy Mater. **7**, 1602888 (2017).

[8] A. Maazaz, C. Delmas, and P. Hagenmuller, A study of the Na_xTiO_2 system by electrochemical deintercalation, J. Inclusion Phenom. **1**, 45 (1983).

[9] D. Wu, X. Li, B. Xu, N. Twu, L. Liu, and G. Ceder, $NaTiO_2$: A layered anode material for sodium-ion batteries, Energy Environ. Sci. **8**, 195 (2015).

[10] C. Didier, M. Guignard, C. Denage, O. Szajwaj, S. Ito, I. Saadoune, J. Darriet, and C. Delmas, Electrochemical Na-deintercalation from $NaVO_2$, Electrochem. Solid-State Lett. **14**, A75 (2011).

[11] J. J. Braconnier, C. Delmas, and P. Hagenmuller, Etude par desintercalation electrochimique des systemes Na_xCrO_2 et Na_xNiO_2, Mater. Res. Bull. **17**, 993 (1982).

[12] S. Miyazaki, S. Kikkawa, and M. Koizumi, Chemical and electrochemical deintercalations of the layered compounds $LiMO_2$ (M = Cr, Co) and $NaM'O_2$ (M' = Cr, Fe, Co, Ni), Synth. Met. **6**, 211 (1983).

[13] S. Komaba, C. Takei, T. Nakayama, A. Ogata, and N. Yabuuchi, Electrochemical intercalation activity of layered $NaCrO_2$ vs. $LiCrO_2$, Electrochem. Commun. **12**, 355 (2010).

[14] A. Mendiboure, C. Delmas, and P. Hagenmuller, Electrochemical intercalation and deintercalation of Na_xMnO_2 bronzes, J. Solid State Chem. **57**, 323 (1985).

[15] X. Ma, H. Chen, and G. Ceder, Electrochemical properties of monoclinic $NaMnO_2$, J. Electrochem. Soc. **158**, A1307 (2011).

[16] Y. Takeda, K. Nakahara, M. Nishijima, N. Imanishi, O. Yamamoto, M. Takano, and R. Kanno, Sodium deintercalation from sodium iron oxide, Mater. Res. Bull. **29**, 659 (1994).

[17] N. Yabuuchi, H. Yoshida, and S. Komaba, Crystal structures and electrode performance of alpha-$NaFeO_2$ for rechargeable sodium batteries, Electrochemistry **80**, 716 (2012).

[18] C. Delmas, J.-J. Braconnier, C. Fouassier, and P. Hagenmuller, Electrochemical intercalation of sodium in Na_xCoO_2 bronzes, Solid State Ionics **3-4**, 165 (1981).

[19] S. Kikkawa, S. Miyazaki, and M. Koizumi, Deintercalated $NaCoO_2$ and $LiCoO_2$, J. Solid State Chem. **62**, 35 (1986).

[20] P. Vassilaras, X. Ma, X. Li, and G. Ceder, Electrochemical properties of monoclinic $NaNiO_2$, J. Electrochem. Soc. **160**, A207 (2013).

[21] S. Komaba, T. Nakayama, A. Ogata, T. Shimizu, C. Takei, S. Takada, A. Hokura, and I. Nakai, Electrochemically reversible sodium intercalation of layered $NaNi_{0.5}Mn_{0.5}O_2$ and $NaCrO_2$, ECS Trans. **16**, 43 (2009).

[22] H. Yoshida, N. Yabuuchi, and S. Komaba, $NaFe_{0.5}Co_{0.5}O_2$ as high energy and power positive electrode for Na-ion batteries, Electrochem. Commun. **34**, 60 (2013).

[23] K. Kubota, T. Asari, H. Yoshida, N. Yaabuuchi, H. Shiiba, M. Nakayama, and S. Komaba, Understanding the structural evolution and redox mechanism of a $NaFeO_2$-$NaCoO_2$ solid solution for sodium-ion batteries, Adv. Funct. Mater. **26**, 6047 (2016).

[24] C.-Y. Yu, J.-S. Park, H.-G. Jung, K.-Y. Chung, D. Aurbach, Y.-K. Sun, and S.-T. Myung, $NaCrO_2$ cathode for high-rate sodium-ion batteries, Energy Environ. Sci. **8**, 2019 (2015).

[25] X. Xia and J. R. Dahn, $NaCrO_2$ is a fundamentally safe positive electrode material for sodium-ion batteries with liquid electrolytes, Electrochem. Solid-State Lett. **15**, A1 (2012).

[26] J. Vinckevičiūtė, M. D. Radin, and A. Van der Ven, Stacking-sequence changes and Na ordering in layered intercalation materials, Chem. Mater. **28**, 8640 (2016).

[27] J. L. Kaufman, J. Vinckevičiūtė, S. K. Kolli, J. G. Goiri, and A. Van der Ven, Understanding intercalation compounds for sodium-ion batteries and beyond, Philos. Trans. R. Soc. A **377**, 20190020 (2019).

[28] S. Mariyappan, Q. Wang, and J. M. Tarascon, Will sodium layered oxides ever be competitive for sodium ion battery applications? J. Electrochem. Soc. **165**, A3714 (2018).

[29] P. R. Elliston, F. Habbal, N. Saleh, G. E. Watson, K. W. Blazey, and H. Rohrer, Magnetic and optical study of $NaCrO_2$, J. Phys. Chem. Solids **36**, 877 (1975).

[30] A. Olariu, P. Mendels, F. Bert, B. G. Ueland, P. Schiffer, R. F. Berger, and R. J. Cava, Unconventional Dynamics in Triangular Heisenberg Antiferromagnet $NaCrO_2$, Phys. Rev. Lett. **97**, 167203 (2006).

[31] D. Hsieh, D. Qian, R. F. Berger, R. J. Cava, J. W. Lynn, Q. Huang, and M. Z. Hasan, Unconventional spin order in the triangular lattice system $NaCrO_2$: A neutron scattering study, Phys. B: Condens. Matter **403**, 1341 (2008).

[32] D. Hsieh, D. Qian, R. F. Berger, R. J. Cava, J. W. Lynn, Q. Huang, and M. Z. Hasan, Magnetic excitations in triangular lattice $NaCrO_2$, J. Phys. Chem. Solids **69**, 3174 (2008).

[33] M. Hemmida, H.-A. Krug von Nidda, N. Büttgen, A. Loidl, L. K. Alexander, R. Nath, A. V. Mahajan, R. F. Berger, R. J. Cava, Y. Singh, and D. C. Johnston, Vortex dynamics and frustration in two-dimensional triangular chromium lattices, Phys. Rev. B **80**, 054406 (2009).

[34] K. Somesh, Y. Furukawa, G. Simutis, F. Bert, M. Prinz-Zwick, N. Büttgen, A. Zorko, A. A. Tsirlin, P. Mendels, and R. Nath, Universal fluctuating regime in triangular chromate antiferromagnets, Phys. Rev. B **104**, 104422 (2021).

[35] M. D. Radin and A. Van der Ven, Stability of prismatic and octahedral coordination in layered oxides and sulfides intercalated with alkali and alkaline-earth metals, Chem. Mater. **28**, 7898 (2016).

[36] M. D. Radin, J. Alvarado, Y. S. Meng, and A. Van der Ven, Role of crystal symmetry in the reversibility of stacking-sequence changes in layered intercalation electrodes, Nano Lett. **17**, 7789 (2017).

[37] K. Kubota, I. Ikeuchi, T. Nakayama, C. Takei, N. Yabuuchi, H. Shiiba, M. Nakayama, and S. Komaba, New insight into structural evolution in layered $NaCrO_2$ during electrochemical sodium extraction, J. Phys. Chem. C **119**, 166 (2015).

[38] Y.-N. Zhou, J.-J. Ding, K.-W. Nam, X. Yu, S.-M. Bak, E. Hu, J. Liu, J. Bai, H. Li, Z.-W. Fu, and X.-Q. Yang, Phase transition behavior of $NaCrO_2$ during sodium extraction studied by synchrotron-based x-ray diffraction and absorption spectroscopy, J. Mater. Chem. A **1**, 11130 (2013).

[39] S.-H. Bo, X. Li, A. J. Toumar, and G. Ceder, Layered-to-rock-salt transformation in desodiated Na_xCrO_2 (x 0.4), Chem. Mater. **28**, 1419 (2016).

[40] C. L. Jakobsen, M. Brighi, B. P. Andersen, G. Ducrest, R. Černý, and D. B. Ravnsbæk, Expanded solid-solution behavior and charge-discharge asymmetry in Na_xCrO_2 Na-ion battery electrodes, J. Power Sources **535**, 231317 (2022).

[41] N. Yabuuchi, I. Ikeuchi, K. Kubota, and S. Komaba, Thermal stability of Na_xCrO_2 for rechargeable sodium batteries: Studies by high-temperature synchrotron x-ray diffraction, ACS Appl. Mater. Interfaces **8**, 32292 (2016).

[42] X. Chen, H. Tang, Y. Wang, and X. Li, Balancing orbital effects and on-site Coulomb repulsion through Na modulations in Na_xVO_2, Phys. Rev. Mater. **5**, 084402 (2021).

[43] A. J. Toumar, S. P. Ong, W. D. Richards, S. Dacek, and G. Ceder, Vacancy Ordering in O3-Type Layered Metal Oxide Sodium-Ion Battery Cathodes, Phys. Rev. Appl. **4**, 064002 (2015).

[44] G. Kresse and J. Hafner, *Ab initio* molecular dynamics for liquid metals, Phys. Rev. B **47**, 558 (1993).

[45] G. Kresse and J. Hafner, *Ab initio* molecular-dynamics simulation of the liquid-metal–amorphous-semiconductor transition in germanium, Phys. Rev. B **49**, 14251 (1994).

[46] G. Kresse and J. Furthmüller, Efficiency of ab-initio total energy calculations for metals and semiconductors using a plane-wave basis set, Comput. Mater. Sci. **6**, 15 (1996).

[47] G. Kresse and J. Furthmüller, Efficient iterative schemes for *ab initio* total-energy calculations using a plane-wave basis set, Phys. Rev. B **54**, 11169 (1996).

[48] P. E. Blöchl, Projector augmented-wave method, Phys. Rev. B **50**, 17953 (1994).

[49] G. Kresse and D. Joubert, From ultrasoft pseudopotentials to the projector augmented-wave method, Phys. Rev. B **59**, 1758 (1999).

[50] H. J. Monkhorst and J. D. Pack, Special points for Brillouin-zone integrations, Phys. Rev. B **13**, 5188 (1976).

[51] P. E. Blöchl, O. Jepsen, and O. K. Andersen, Improved tetrahedron method for Brillouin-zone integrations, Phys. Rev. B **49**, 16223 (1994).

[52] J. Sun, A. Ruzsinszky, and J. P. Perdew, Strongly Constrained and Appropriately Normed Semilocal Density Functional, Phys. Rev. Lett. **115**, 036402 (2015).

[53] J. Sun, R. C. Remsing, Y. Zhang, Z. Sun, A. Ruzsinszky, H. Peng, Z. Yang, A. Paul, U. Waghmare, X. Wu, M. L. Klein, and J. P. Perdew, Accurate first-principles structures and energies of diversely bonded systems from an efficient density functional, Nat. Chem. **8**, 831 (2016).

[54] H. Kim, D.-H. Seo, A. Urban, J. Lee, D.-H. Kwon, S.-H. Bo, T. Shi, J. K. Papp, B. D. McCloskey, and G. Ceder, Stoichiometric layered potassium transition metal oxide for rechargeable potassium batteries, Chem. Mater. **30**, 6532 (2018).

[55] A. Chakraborty, M. Dixit, D. Aurbach, and D. T. Major, Predicting accurate cathode properties of layered oxide materials using the SCAN meta-GGA density functional, npj Comput. Mater. **4**, 60 (2018).

[56] D. A. Kitchaev, H. Peng, Y. Liu, J. Sun, J. P. Perdew, and G. Ceder, Energetics of MnO_2 polymorphs in density functional theory, Phys. Rev. B **93**, 045132 (2016).

[57] J. H. Yang, D. A. Kitchaev, and G. Ceder, Rationalizing accurate structure prediction in the meta-GGA SCAN functional, Phys. Rev. B **100**, 035132 (2019).

[58] J. L. Kaufman and A. Van der Ven, Ordering and structural transformations in layered K_xCrO_2 for K-ion batteries, Chem. Mater. **32**, 6392 (2020).

[59] D. A. Kitchaev, J. Vinckeviciute, and A. Van der Ven, Delocalized metal-oxygen π-redox is the origin of anomalous nonhysteretic capacity in Li-ion and Na-ion cathode materials, J. Am. Chem. Soc. **143**, 1908 (2021).

[60] J. Vinckeviciute, D. A. Kitchaev, and A. Van der Ven, A two-step oxidation mechanism controlled by Mn migration explains the first-cycle activation behavior of Li_2MnO_3-based Li-excess materials, Chem. Mater. **33**, 1625 (2021).

[61] J. P. Perdew, K. Burke, and M. Ernzerhof, Generalized Gradient Approximation Made Simple, Phys. Rev. Lett. **77**, 3865 (1996).

[62] S. L. Dudarev, G. A. Botton, S. Y. Savrasov, C. J. Humphreys, and A. P. Sutton, Electron-energy-loss spectra and the structural stability of nickel oxide: An LSDA+U study, Phys. Rev. B **57**, 1505 (1998).

[63] K. Momma and F. Izumi, VESTA 3 for three-dimensional visualization of crystal, volumetric and morphology data, J. Appl. Crystallogr. **44**, 1272 (2011).

[64] CASM: A Clusters Approach to Statistical Mechanics, https://github.com/prisms-center/CASMcode.

[65] A. Van der Ven, J. C. Thomas, B. Puchala, and A. R. Natarajan, First-principles statistical mechanics of multicomponent crystals, Annu. Rev. Mater. Res. **48**, 27 (2018).

[66] J. C. Thomas and A. Van der Ven, Finite-temperature properties of strongly anharmonic and mechanically unstable crystal phases from first principles, Phys. Rev. B **88**, 214111 (2013).

[67] B. Puchala and A. Van der Ven, Thermodynamics of the Zr-O system from first-principles calculations, Phys. Rev. B **88**, 094108 (2013).

[68] See Supplemental Material at http://link.aps.org/supplemental/10.1103/PhysRevMaterials.6.115401 for details of cluster expansions and Monte Carlo simulations, link to DFT data, hull distances of calculated configurations, results of magnetic calculations, energies of different stackings of P3 orderings, spinel crystal structure, summary of parameters from experimental literature, and comparison of results from different DFT methods.

[69] G. L. W. Hart, V. Blum, M. J. Walorski, and A. Zunger, Evolutionary approach for determining first-principles Hamiltonians, Nat. Mater. **4**, 391 (2005).

[70] A. van de Walle and M. Asta, Self-driven lattice-model Monte Carlo simulations of alloy thermodynamic properties and phase diagrams, Modell. Simul. Mater. Sci. Eng. **10**, 521 (2002).

[71] A. S. Dalton, A. A. Belak, and A. Van der Ven, Thermodynamics of lithium in TiO_2(B) from first principles, Chem. Mater. **24**, 1568 (2012).

[72] A. Van der Ven, Z. Deng, S. Banerjee, and S. P. Ong, Rechargeable alkali-ion battery materials: Theory and computation, Chem. Rev. **120**, 6977 (2020).

[73] A. R. Natarajan and A. Van der Ven, Toward an understanding of deformation mechanisms in metallic lithium and sodium from first-principles, Chem. Mater. **31**, 8222 (2019).

[74] E. Pavarini, E. Koch, F. Anders, and M. Jarrell, *Correlated Electrons: From Models to Materials*, Tech. Rep. (Forschungszentrum Jülich GmbH Zenralbibliothek, Verlag Jülich, 2012).

[75] J. L. Kaufman and A. Van der Ven, Na_xCoO_2 phase stability and hierarchical orderings in the O3/P3 structure family, Phys. Rev. Mater. **3**, 015402 (2019).

[76] Q. Huang, M. L. Foo, J. W. Lynn, H. W. Zandbergen, G. Lawes, Y. Wang, B. H. Toby, A. P. Ramirez, N. P. Ong, and R. J. Cava, Low temperature phase transitions and crystal structure of $Na_{0.5}CoO_2$, J. Phys.: Condens. Matter **16**, 5803 (2004).

[77] M. Guignard, C. Didier, J. Darriet, P. Bordet, E. Elkaïm, and C. Delmas, P2-Na_xVO_2 system as electrodes for batteries and electron-correlated materials, Nat. Mater. **12**, 74 (2013).

[78] M. Y. Toriyama, J. L. Kaufman, and A. Van der Ven, Potassium ordering and structural phase stability in layered K_xCoO_2, ACS Appl. Energy Mater. **2**, 2629 (2019).

[79] A. Van der Ven, G. Ceder, M. Asta, and P. D. Tepesch, First-principles theory of ionic diffusion with nondilute carriers, Phys. Rev. B **64**, 184307 (2001).

[80] A. Van der Ven, J. C. Thomas, Q. Xu, B. Swoboda, and D. Morgan, Nondilute diffusion from first principles: Li diffusion in Li_xTiS_2, Phys. Rev. B **78**, 104306 (2008).

[81] A. Van der Ven, J. Bhattacharya, and A. A. Belak, Understanding Li diffusion in Li-intercalation compounds, Acc. Chem. Res. **46**, 1216 (2013).

[82] X. Li, Y. Wang, D. Wu, L. Liu, S.-H. Bo, and G. Ceder, Jahn-Teller assisted Na diffusion for high performance Na ion batteries, Chem. Mater. **28**, 6575 (2016).

[83] W. H. Kan, B. Deng, Y. Xu, A. K. Shukla, T. Bo, S. Zhang, J. Liu, P. Pianetta, B.-T. Wang, Y. Liu, and G. Chen, Understanding the effect of local short-range ordering on lithium diffusion in $Li_{1.3}Nb_{0.3}Mn_{0.4}O_2$ single-crystal cathode, Chem **4**, 2108 (2018).

[84] H. Ji, A. Urban, D. A. Kitchaev, D.-H. Kwon, N. Artrith, C. Ophus, W. Huang, Z. Cai, T. Shi, J. C. Kim, H. Kim, and G.

Ceder, Hidden structural and chemical order controls lithium transport in cation-disordered oxides for rechargeable batteries, Nat. Commun. **10**, 592 (2019).

[85] R. J. Clément, Z. Lun, and G. Ceder, Cation-disordered rocksalt transition metal oxides and oxyfluorides for high energy lithium-ion cathodes, Energy Environ. Sci. **13**, 345 (2020).

[86] Z. Lun, B. Ouyang, D.-H. Kwon, Y. Ha, E. E. Foley, T.-Y. Huang, Z. Cai, H. Kim, M. Balasubramanian, Y. Sun, J. Huang, Y. Tian, H. Kim, B. D. McCloskey, W. Yang, R. J. Clément, H. Ji, and G. Ceder, Cation-disordered rocksalt-type high-entropy cathodes for Li-ion batteries, Nat. Mater. **20**, 214 (2021).

[87] J. L. Kaufman and A. Van der Ven, Antiphase boundary migration as a diffusion mechanism in a P3 sodium layered oxide, Phys. Rev. Mater. **5**, 055401 (2021).

[88] A. Jain, G. Hautier, S. P. Ong, C. J. Moore, C. C. Fischer, K. A. Persson, and G. Ceder, Formation enthalpies by mixing GGA and GGA+U calculations, Phys. Rev. B **84**, 045115 (2011).

[89] Y. Hinuma, Y. S. Meng, and G. Ceder, Temperature-concentration phase diagram of P2-Na$_x$CoO$_2$ from first-principles calculations, Phys. Rev. B **77**, 224111 (2008).

[90] J. W. Furness, A. D. Kaplan, J. Ning, J. P. Perdew, and J. Sun, Accurate and numerically efficient r^{2}SCAN meta-generalized gradient approximation, J. Phys. Chem. Lett. **11**, 8208 (2020).

[91] J. Ning, J. W. Furness, and J. Sun, Reliable lattice dynamics from an efficient density functional approximation, Chem. Mater. **34**, 2562 (2022).

[92] J. L. Kaufman and A. Van der Ven, Cation diffusion facilitated by antiphase boundaries in layered intercalation compounds, Chem. Mater. **34**, 1889 (2022).